Supplement of

Chemical characterization of oxygenated organic compounds in gas-phase and particle-phase using iodide-CIMS with FIGAERO in urban air

Chenshuo Ye[1], Bin Yuan[2,3,*], Yi Lin[2,3], Zelong Wang[2,3], Weiwei Hu[4], Tiange Li[2,3], Wei Chen[4], Caihong Wu[2,3], Chaomin Wang[2,3], Shan Huang[2,3], Jipeng Qi[2,3], Baolin Wang[5], Chen Wang[5], Wei Song[4], Xinming Wang[4], E Zheng[2,3], Jordan E. Krechmer[6], Penglin Ye[7], Zhanyi Zhang[2,3], Xuemei Wang[2,3], Douglas R. Worsnop[6], Min Shao[2,3,1,*]

[1] College of Environmental Sciences and Engineering, Peking University, Beijing 100871, China

[2] Institute for Environmental and Climate Research, Jinan University, Guangzhou 511443, China

[3] Guangdong-Hongkong-Macau Joint Laboratory of Collaborative Innovation for Environmental Quality, Guangzhou 511443, China

[4] Guangzhou Institute of Geochemistry, Chinese Academy of Sciences, Guangzhou 511443, China

[5] School of Environmental Science and Engineering, Qilu University of Technology, Jinan 250353, China

[6] Aerodyne Research, Inc. 45 Manning Rd., Billerica, MA, USA

[7] Shanghai Key Laboratory of Atmospheric Particle Pollution and Prevention (LAP[3]), Department of Environmental Science and Engineering, Fudan University, Shanghai 200438, China

*Correspondence to: byuan@jnu.edu.cn; mshao@pku.edu.cn

Section S1. Determination of response factors for uncalibrated species

The concentration of one species A is calculated as:

$$[A] = \frac{signal}{response\ factor} = \frac{signal}{\left(S_{max} * \frac{1}{S_0}\right) * relTrans}$$

The response factors of iodide adducts are determined via determining

(a) $\frac{1}{S_0}$: sensitivity of species A relative to maximum sensitivity, S_{max};

(b) $relTrans$: relative transmission of species A, i.e., transmission efficiency of species A relative to primary ions.

1.1 Relative sensitivity

Previous work has verified the connections among the binding energy of the iodide-adduct bond, the voltage dissociating iodide adducts and the sensitivity of corresponding species (Iyer et al., 2016; Lopez-Hilfiker et al., 2016). First, we performed the voltage scanning procedure on the gases during different time of day: morning, afternoon, evening and night. Then we used sigmoidal function with constrains to fit the fraction of remaining signal and dV which is the voltage difference of the interface between two quadrupoles in CIMS. Every fit of an individual iodide adduct yielded two parameters: S_0, the relative signal at much weaker dV compared to the signal under operational dV; dV_{50}, the voltage at which half of the signal is removed (i.e. half of an iodide adduct dissociate). We constrained that S_0 should be larger than 0.9 and dV_{50} should be less than 50. We averaged reasonable results of inverse S_0 and dV_{50} for every iodide adduct. After removing outliers (Motulsky and Brown, 2006), we applied sigmoidal fit to the results of individual fits of all the iodide adducts and obtained an empirical relationship between relative sensitivity and dV_{50}. As shown in Fig. S7a, our result is very similar to the curve reported in Lopez-Hilfiker et al., 2016. There are 107 of 1334 iodide adducts that we failed to obtain dV_{50}, so we assume that they have a relative sensitivity of 0.23 which is the left limit of sigmoidal curve in Fig. S7a.

We took the calibration factor of levoglucosan, 60 ncps/ppt, as the maximum sensitivity. On the one hand, levoglucosan is one of the compounds that we calibrated

most frequently; on the other hand, it is one of the maximum sensitivity compounds (Iyer et al., 2016) and has a transmission efficiency very close to primary ions (see Sect. 1.2). The possible reason why the iodide cluster of $C_6H_{10}O_5$ had a relative sensitivity lower than one is that it included isomers which were weakly bonded with iodide. Sensitivities derived from voltage scanning for gaseous species would be applied to particle-phase species, as discussed in the supplement file of Isaacman-VanWertz et al., 2018.

1.2 Relative transmission efficiency

Transmission efficiency of an ion in CIMS instrument depends on its mass-to-charge ratio. Known compounds across the m/z range of interest were introduced into the CIMS one by one and the relative transmission as a function of m/z was determined via comparing the increase of analyte ions relative to the decrease of primary ions (Heinritzi et al., 2016). Compounds used for this calibration were formic acid, acetic acid, lactic acid and C2-C5 perfluorinated acids ($C_2HF_3O_2$, $C_3HF_5O_2$, $C_4HF_7O_2$, $C_5HF_9O_2$). The gaussian function was applied for fitting this dependence curve as shown in Fig. S7b.

The final response factors for iodide adducts are plotted in Fig. S7c. For 35 species that we had calibrated, response factors derived were replaced by calibration factors when converting their signals to concentrations.

Section S2. $\overline{OS_C}$ of a $C_xH_yO_z$ and $C_xH_yN_{1,2}O_z$ compound

The $\overline{OS_C} - n_C$ space which plots $\overline{OS_C}$ as the function of carbon number, provides a framework for describing the bulk chemical properties and the evolution of organics (Kroll et al., 2011). The approximate $\overline{OS_C}$ of a $C_xH_yO_z$ compound was calculated as:

$$\overline{OS_C} = 2 \times \frac{O}{C} - \frac{H}{C} \quad (3)$$

For $C_xH_yN_{1,2}O_z$ compounds, the influence of N is dependent on functional groups so we made several assumptions to classify them. (1) N-containing functional groups are nitro (-NO_2) or nitrate (-NO_3) in our case; (2) N-containing aromatics feature nitro moieties and N-containing aliphatic hydrocarbons feature nitrate moieties; (3) N-

containing aromatics have 6-9 carbon atoms and less hydrogen atoms than aliphatic hydrocarbons with the same carbon atoms. This was not an absolutely right classification but at least it provided a rough separation between nitro compounds and nitrate compounds for most $C_xH_yN_{1,2}O_z$ species. After the above step, $3 \times \frac{N}{C}$ and $5 \times \frac{N}{C}$ was minus from equation (3) for nitro compounds and for nitrate compounds, respectively:

$$\overline{OS_C} = 2 \times \frac{O}{C} - \frac{H}{C} - (3\ or\ 5) \times \frac{N}{C} \quad (4)$$

References

Heinritzi, M., Simon, M., Steiner, G., Wagner, A. C., Kürten, A., Hansel, A. and Curtius, J.: Characterization of the mass-dependent transmission efficiency of a CIMS, Atmos. Meas. Tech., 9(4), 1449–1460, doi:10.5194/amt-9-1449-2016, 2016.

Isaacman-VanWertz, G., Massoli, P., O'Brien, R., Lim, C., Franklin, J., Moss, J., Hunter, J., Nowak, J., Canagaratna, M., Misztal, P., Arata, C., Roscioli, J., Herndon, S., Onasch, T., Lambe, A., Jayne, J., Su, L., Knopf, D., Goldstein, A., Worsnop, D. and Kroll, J.: Chemical evolution of atmospheric organic carbon over multiple generations of oxidation, Nat. Chem., 10(4), 462–468, doi:10.1038/s41557-018-0002-2, 2018.

Iyer, S., Lopez-Hilfiker, F., Lee, B. H., Thornton, J. A. and Kurtén, T.: Modeling the Detection of Organic and Inorganic Compounds Using Iodide-Based Chemical Ionization, J. Phys. Chem. A, 120(4), 576–587, doi:10.1021/acs.jpca.5b09837, 2016.

Kroll, J. H., Donahue, N. M., Jimenez, J. L., Kessler, S. H., Canagaratna, M. R., Wilson, K. R., Altieri, K. E., Mazzoleni, L. R., Wozniak, A. S., Bluhm, H., Mysak, E. R., Smith, J. D., Kolb, C. E. and Worsnop, D. R.: Carbon oxidation state as a metric for describing the chemistry of atmospheric organic aerosol, Nat. Chem., 3(2), 133–139, doi:10.1038/nchem.948, 2011.

Lopez-Hilfiker, F. D., Mohr, C., Ehn, M., Rubach, F., Kleist, E., Wildt, J., Mentel, T. F. and Carrasquillo, A. J.: Phase partitioning and volatility of secondary organic aerosol components formed from α -pinene ozonolysis and OH oxidation : the

109 importance of accretion products and other low volatility compounds, Atmos. Chem.
110 Phys., 15, 7765–7776, doi:10.5194/acp-15-7765-2015, 2015.
111 Lopez-Hilfiker, F. D., Iyer, S., Mohr, C., Lee, B. H., Ambro, E. L. D., Kurtén, T. and
112 Thornton, J. A.: Constraining the sensitivity of iodide adduct chemical ionization
113 mass spectrometry to multifunctional organic molecules using the collision limit and
114 thermodynamic stability of iodide ion adducts, Atmos. Meas. Tech., 9, 1505–1512,
115 doi:10.5194/amt-9-1505-2016, 2016.
116 Motulsky, H. J. and Brown, R. E.: Detecting outliers when fitting data with nonlinear
117 regression - A new method based on robust nonlinear regression and the false
118 discovery rate, BMC Bioinformatics, 7, 1–20, doi:10.1186/1471-2105-7-123, 2006.
119 Wu, C., Wang, C., Wang, S., Wang, W., Yuan, B., Qi, J., Wang, B., Wang, H., Wang,
120 C., Song, W., Wang, X., Hu, W., Lou, S., Ye, C., Peng, Y., Wang, Z., Huangfu, Y.,
121 Xie, Y., Zhu, M., Zheng, J., Wang, X., Jiang, B., Zhang, Z. and Shao, M.: Important
122 contributions of oxygenated compounds to emissions and chemistry of VOCs in urban
123 air, Atmos. Chem. Phys. Discuss., 2020, 1–37, doi:10.5194/acp-2020-152, 2020.
124 Yatavelli, R. L. N., Mohr, C., Stark, H., Day, D. A., Thompson, S. L., Lopez-Hilfiker,
125 F. D., Campuzano-Jost, P., Palm, B. B., Vogel, A. L., Hoffmann, T., Heikkinen, L.,
126 Äijälä, M., Ng, N. L., Kimmel, J. R., Canagaratna, M. R., Ehn, M., Junninen, H.,
127 Cubison, M. J., Petäjä, T., Kulmala, M., Jayne, J. T., Worsnop, D. R. and Jimenez, J.
128 L.: Estimating the contribution of organic acids to northern hemispheric continental
129 organic aerosol, Geophys. Res. Lett., 42(14), 6084–6090,
130 doi:10.1002/2015GL064650, 2015.
131
132

133 **Table S1.** The calibrated species and corresponding calibration methods

No.	Calibrated species	Calibration method
1	Chlorine, Hydrogen cyanide	Gaseous standard dilution
2	Formic acid, Acetic acid, Propionic acid, Butyric acid, Pentanoic acid, Catechol, Acrylic acid, Glycollic acid, Lactic acid, Phenol, m-cresol, 4-nitrophenol, 2,4-dinitrophenol, cis-pinonic acid, 3-Methylcatechol, Pyruvic acid	Dissolve standards in the water; Thermally evaporate aqueous standards via the liquid calibration unit (LCU, Ionicon Analytic GmbH) to generate a flow at defined trace concentrations; Liquid standard dilutino
3	Nitric acid, Formic acid	Inject a constant flow into the permeation tube; Dilute the outflow gradiently when its concentration is stable
4	Isocyanic acid, Dinitrogen pentoxide	Use the flow tube reactor to generate the flow containing target compounds; Gas-phase standard dilution
5	Malonic acid, Succinic acid, Meso-erythritol, Glutaric acid, Adipic acid, Pimelic acid, Levoglucosan, Tricarballylic acid, Azelaic acid, Sebacic acid, Dodecanedioic acid, Citric acid, Dipentaerythritol, 4-nitrocatechol, Xylitol, Heptaethylene glycol, Octaethylene glycol	Dissolve standards in organic solvents (e.g., acetone, isopropanol); Inject different amounts of solution on the FIGAERO filter

134

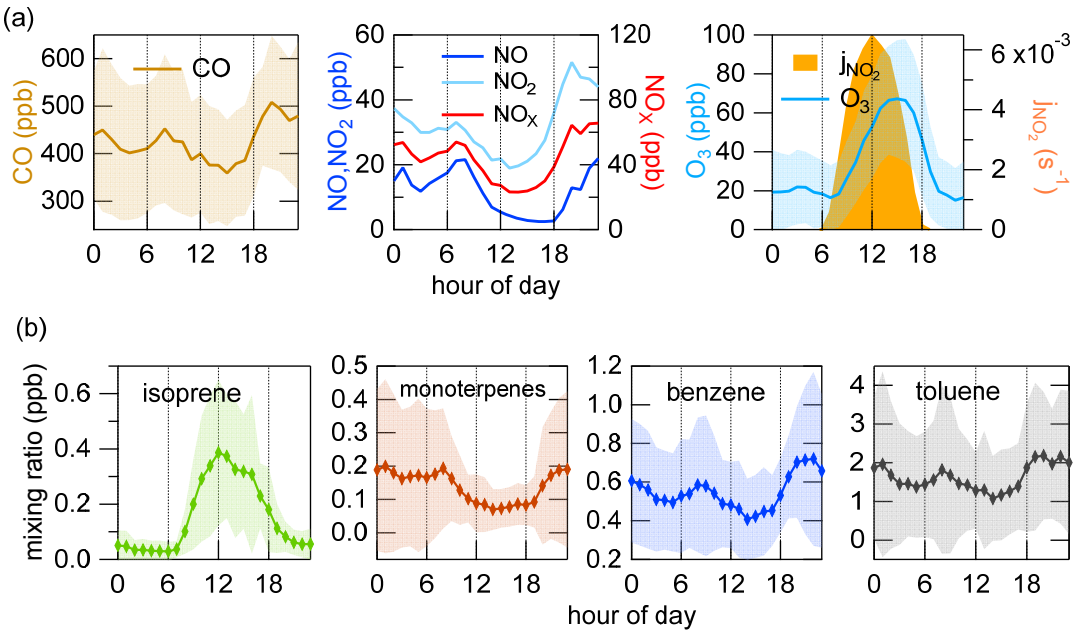

135

136 **Figure S1.** Diurnal trends of trace gases (a) and some important VOCs (b) (Wu et al.,

137 2020). The shading indicates standard deviations.

138

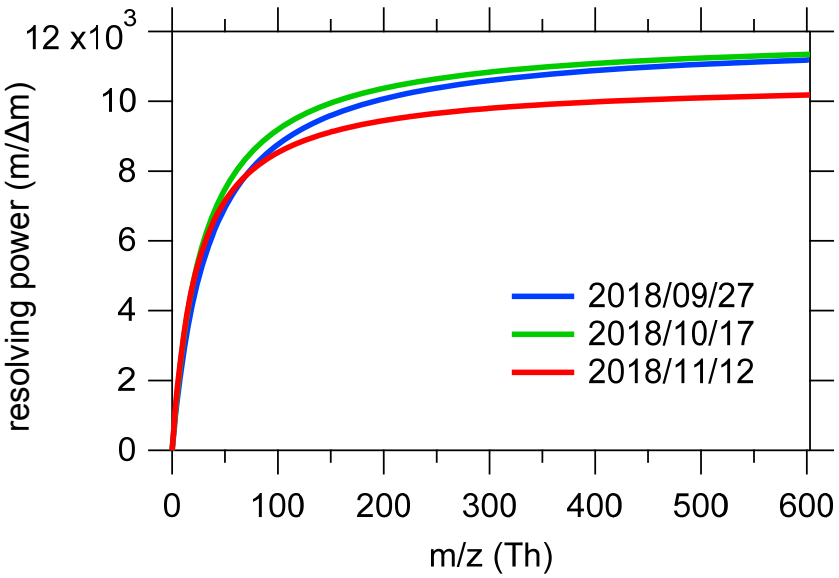

Figure S2. Resolving power of the time-of-flight analyzer as a function of m/z in the beginning, in the middle and in the end of the campaign.

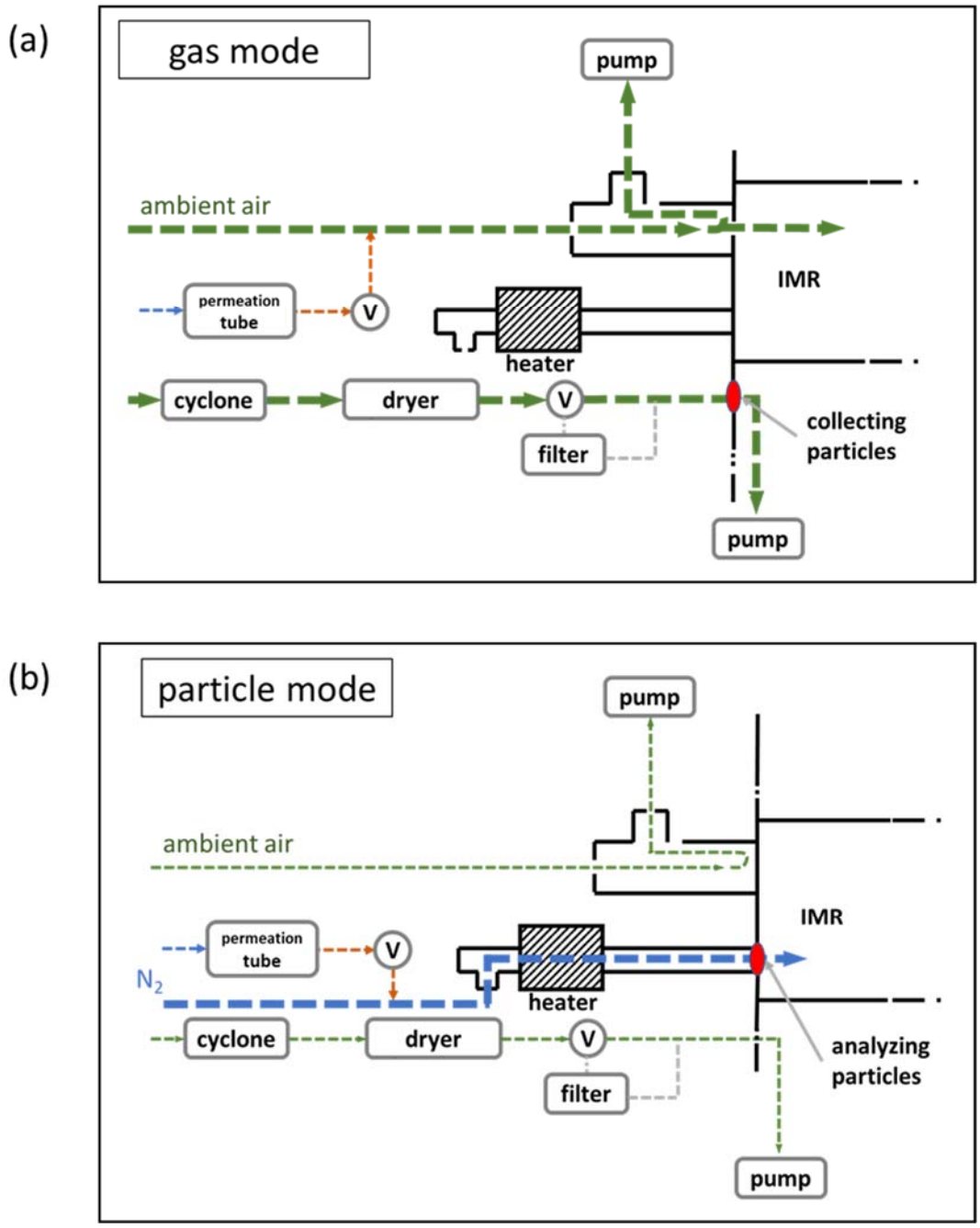

142

143 **Figure S3.** Experimental setups for (a) gas mode in which the instrument
144 simultaneously measures gaseous compounds and collects particles and for (b) particle
145 mode in which collected particles undergo through thermal desorption and analysis.

146

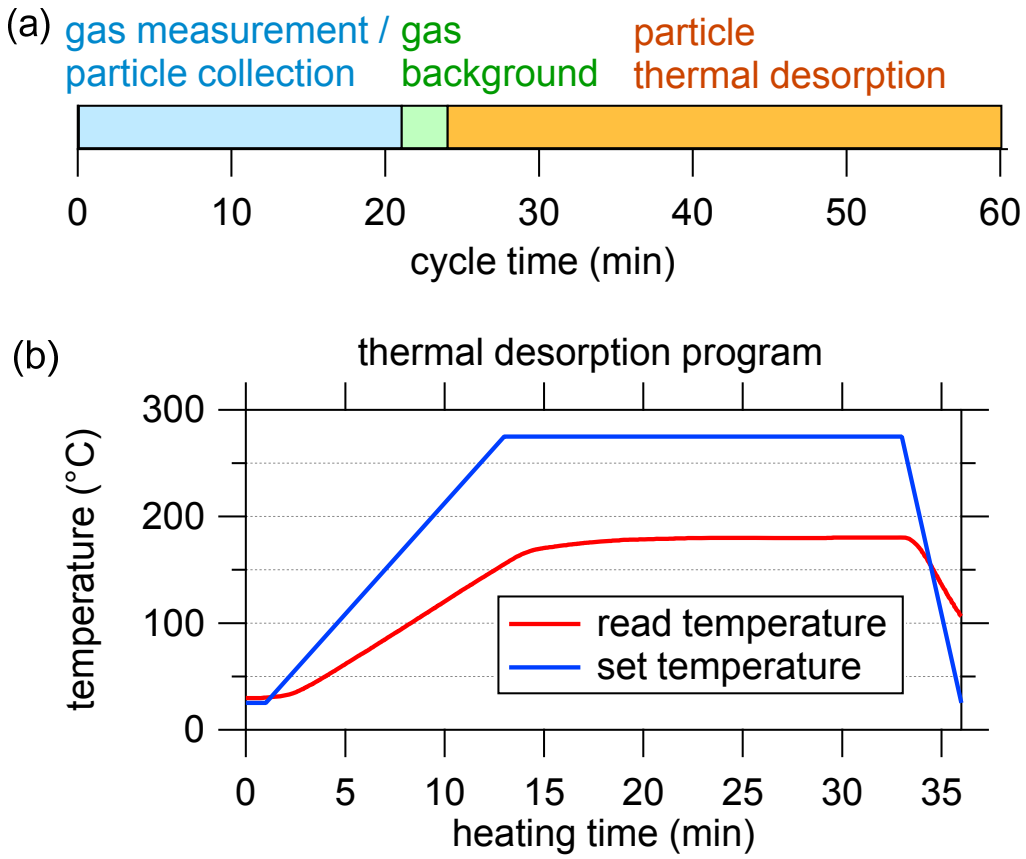

Figure S4. Schematic diagram of cycle modes (a) and FIGAERO heating temperature profile (b).

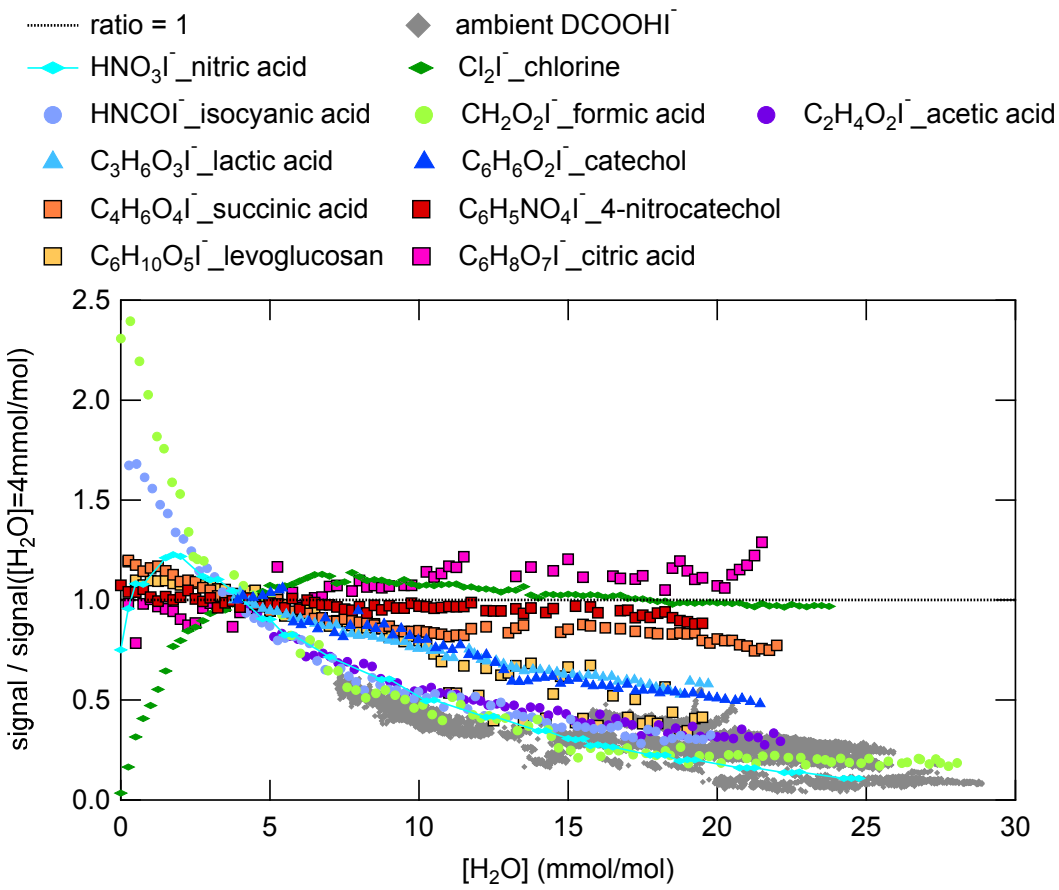

Figure S5. The effects of water content on the sensitivities of different species. The curves with square markers were obtained from calibrations using FIGAERO. Gray dots show how the signal of internal standard DCOOH varied with ambient humidity.

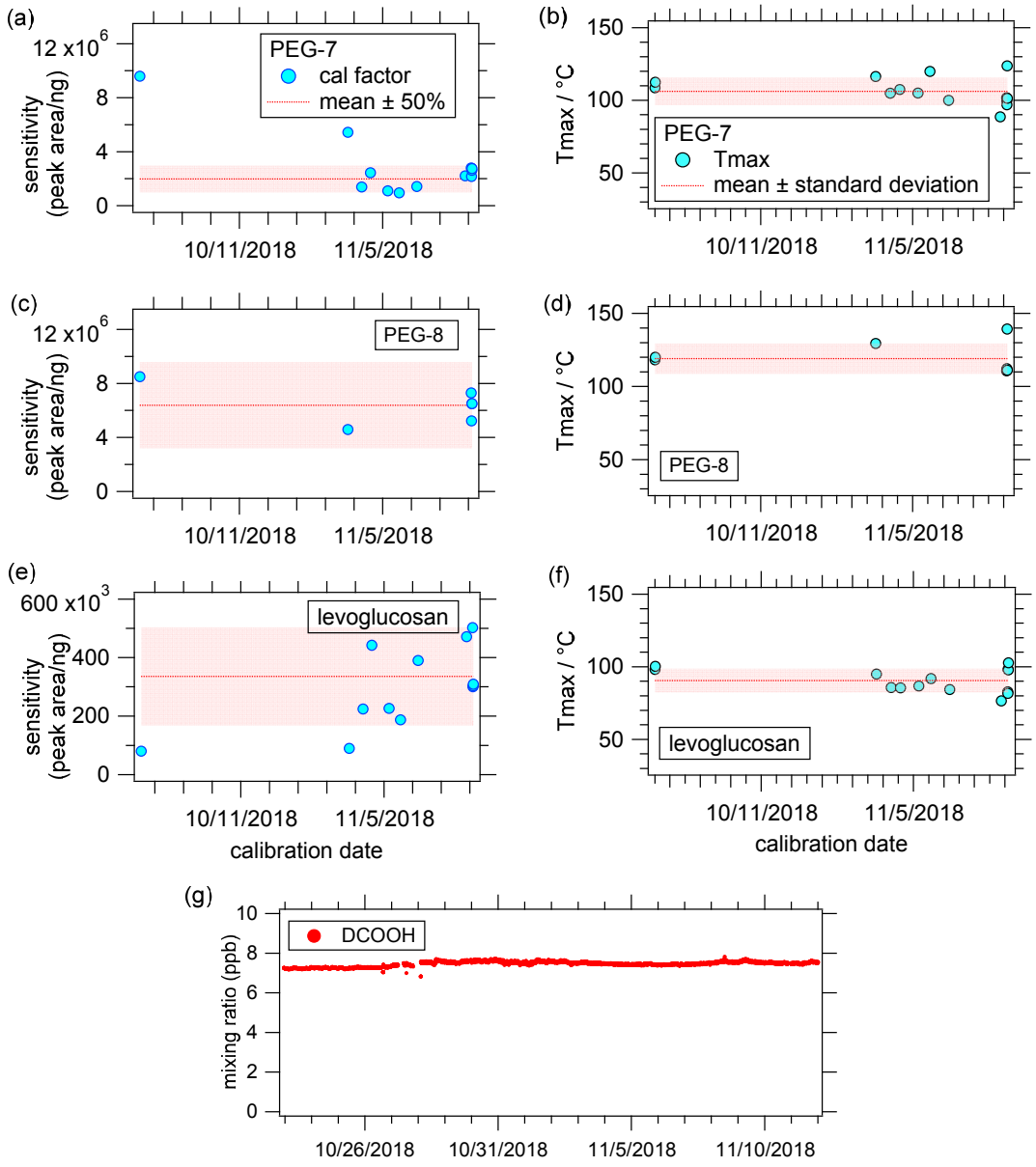

Figure S6. The time series of calibration factors (a, c, e) and T_{max} (b, d, f) of hepaethylene glycol, octaethylene glycol and levoglucosan in the regular calibrations during the campaign. The concentration of levoglucosan was too high in the solution used in the first two calibrations, resulting the deviation of these two calibration factors. (g) The measured concentration of DCOOH was steady after applying humidity correction to the signal of DCOOH based on its curve shown in Fig. S5.

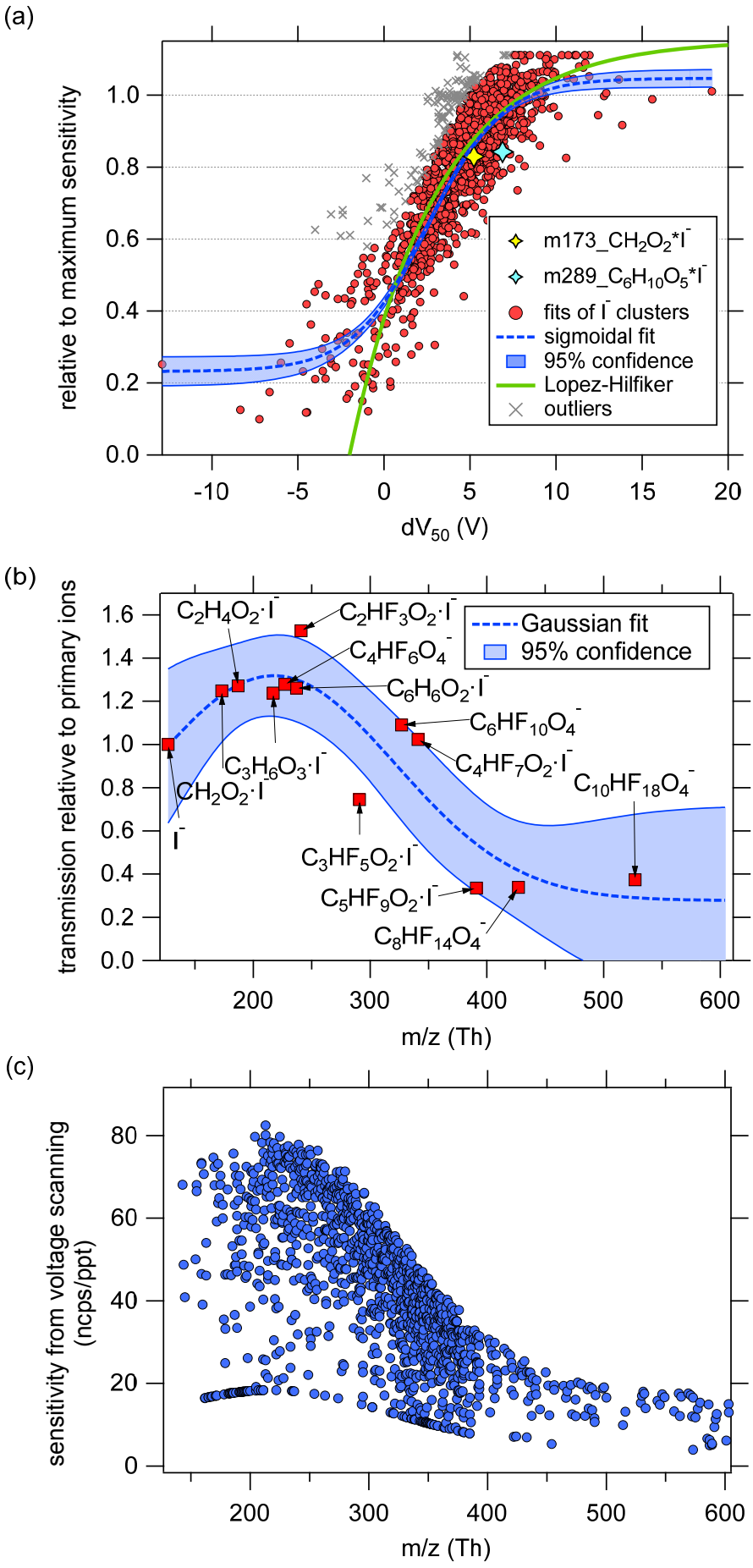
(a)
relative to maximum sensitivity
dV50 (V)
m173_CH2O2*I-
m289_C6H10O5*I-
fits of I- clusters
sigmoidal fit
95% confidence
Lopez-Hilfiker
outliers
(b)
transmission relative to primary ions
m/z (Th)
Gaussian fit
95% confidence
C2H4O2·I-
C2HF3O2·I-
C4HF6O4-
C6H6O2·I-
C6HF10O4-
C4HF7O2·I-
C10HF18O4-
C3H6O3·I-
CH2O2·I-
I-
C3HF5O2·I-
C5HF9O2·I-
C8HF14O4-
(c)
sensitivity from voltage scanning (ncps/ppt)
m/z (Th)

Figure S7. (a) Fitting the voltage scanning results as a sigmoidal function of sensitivity relative to maximum sensitivity versus dV_{50} (i.e. the voltage where half of an iodide adducts dissociate). (b) Fitting relative transmission efficiency as a gaussian curve of m/z. (c) The sensitivity derived from voltage scanning procedure. The transmission correction has been applied. The bottom line in Figure S7c that has a shape exactly the same as the transmission curve represents the points with a cutoff of 0.23 for the relative sensitivity. See text in Section S1.

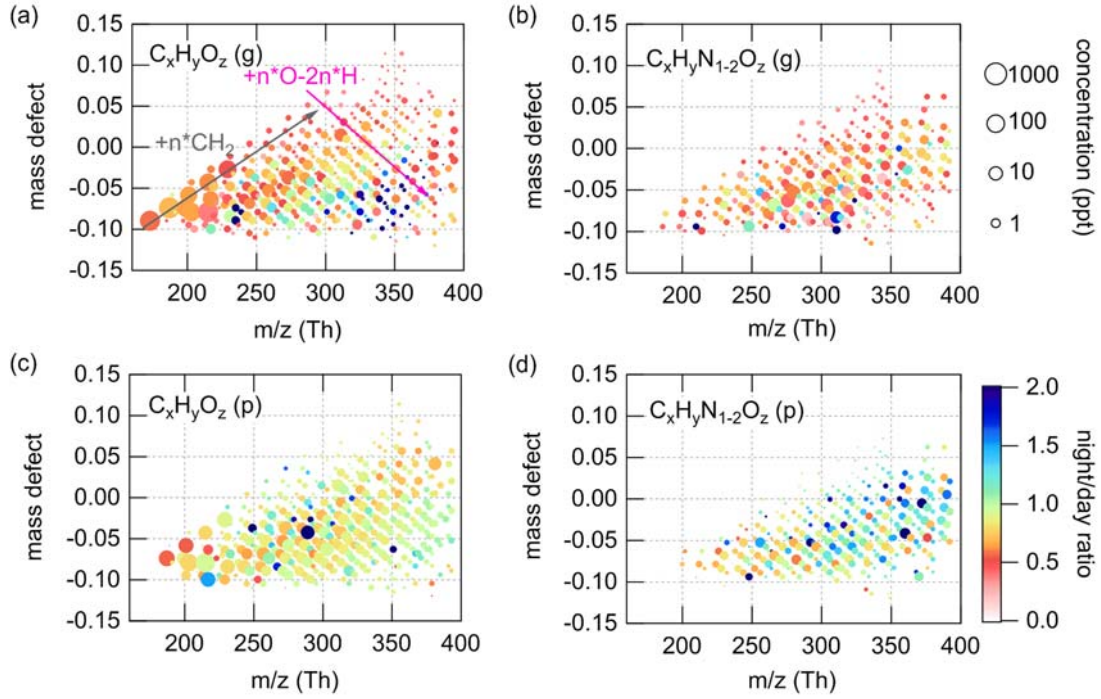

Figure S8. Mass defect diagram for iodide charged $C_xH_yO_z$ compounds in the gas phase (a) and particle phase (c), and $C_xH_yN_{1,2}O_z$ compounds in both phases (b, d). The circle size denotes the concentration and the circle color denotes the ratio of the average nighttime concentration (10 pm to 6 am) to average daytime concentration (10 am to 6 pm).

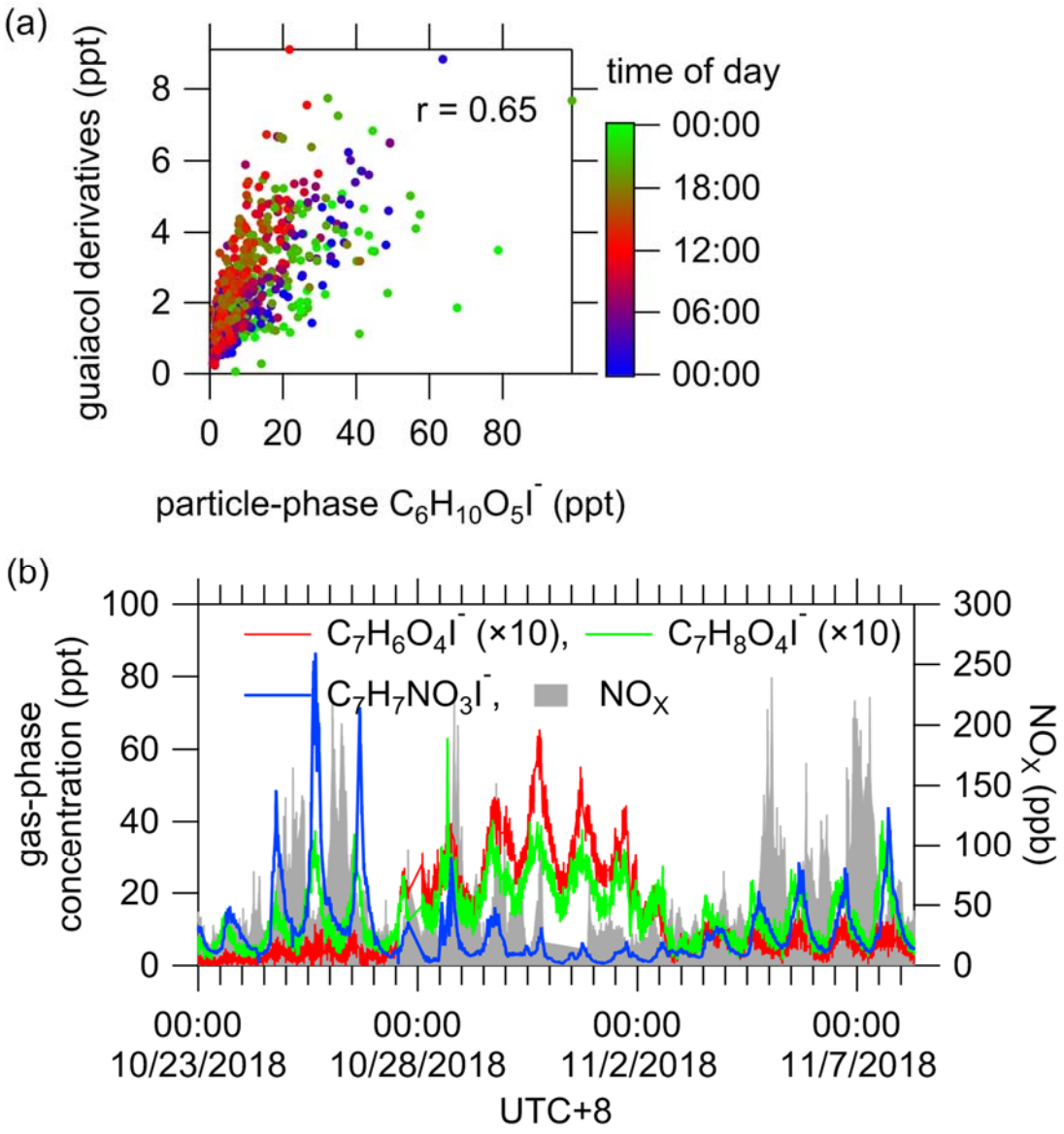

Figure S9. (a) Correlation between guaiacol derivatives ($C_7H_8O_2$, $C_8H_{10}O_2$, $C_9H_{12}O_2$, $C_8H_8O_3$, $C_{10}H_{12}O_2$, $C_9H_{10}O_3$, $C_8H_8O_4$, $C_{10}H_{10}O_3$, $C_{10}H_{12}O_3$, $C_{10}H_{14}O_3$, $C_9H_{10}O_4$, $C_{10}H_{14}O_3$) and levoglucosan ($C_6H_{10}O_5$) in the particle phase. (b) Time series of gaseous $C_7H_6O_4I^-$, $C_7H_8O_4I^-$, $C_7H_7NO_3I^-$ and NO_X.

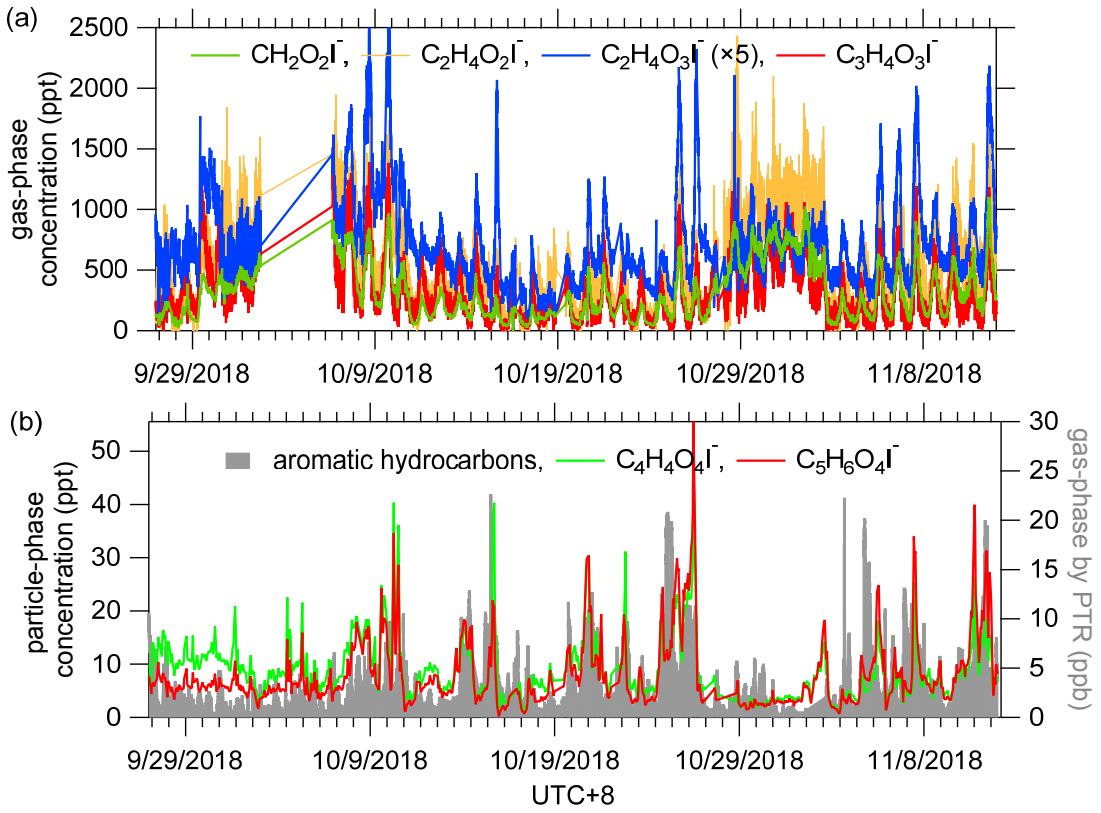

Figure S10. (a) Time series of low-molecular-weight organic acids in gas-phase. (b) Time series of particle-phase $C_4H_4O_4I^-$, $C_5H_6O_4I^-$ and gaseous aromatic hydrocarbons including benzene, toluene, styrene and xylene.

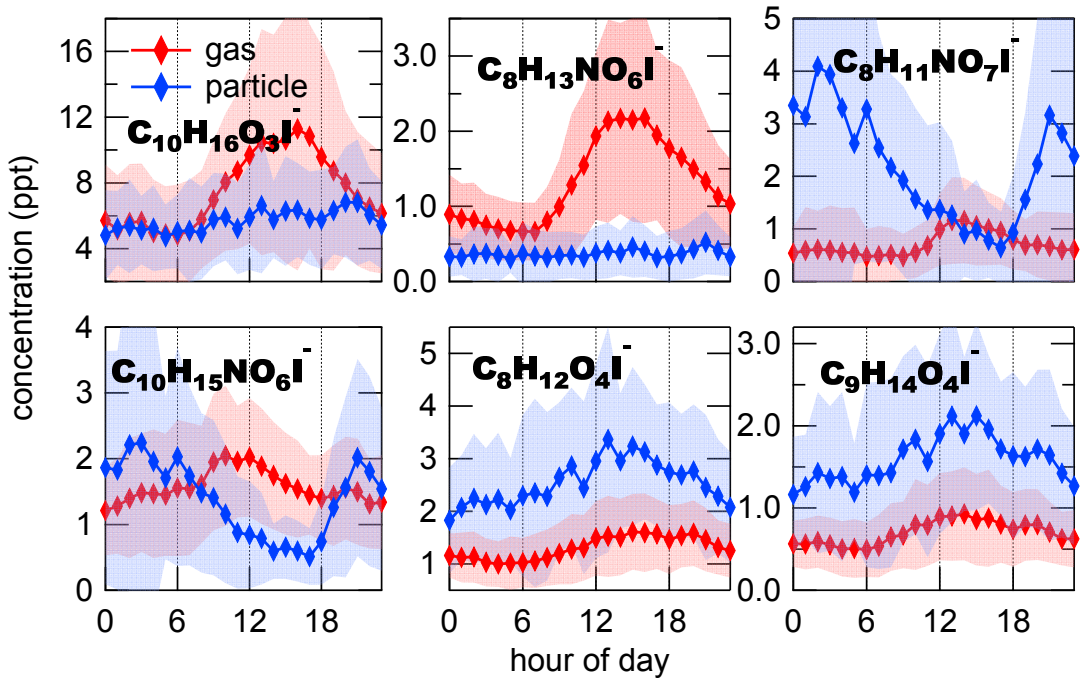

187

188 **Figure S11.** Diurnal variations of oxidation products of monoterpene in the gas phase

189 (red) and particle phase (blue). The shaded areas indicate standard deviations.

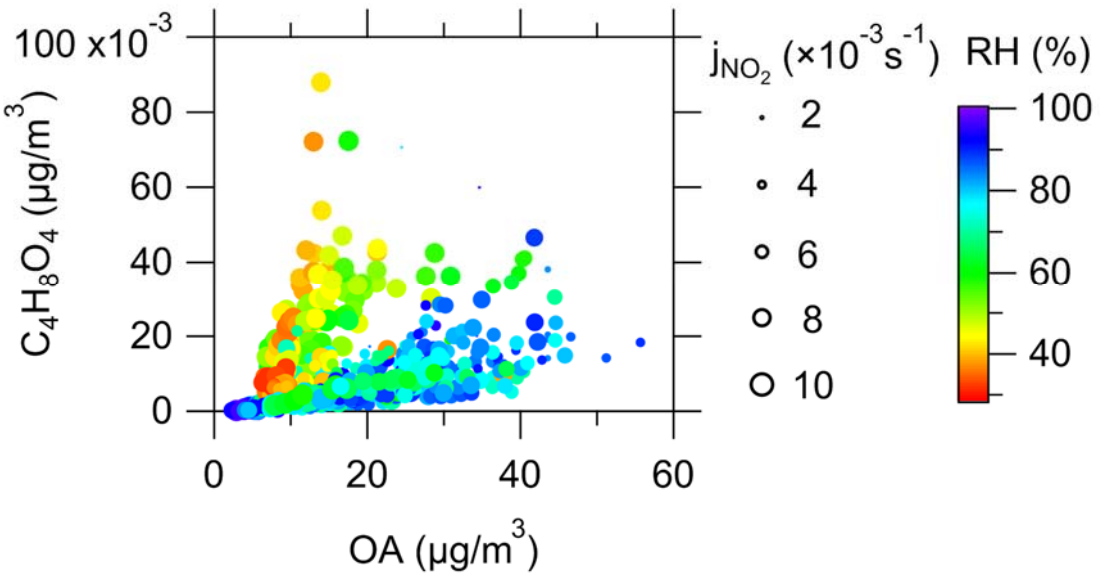

Figure S12. Scatterplot between particle-phase $C_4H_8O_4$ and OA color-coded by ambient RH and size binned by the daily maximums of photolysis rates of NO_2.

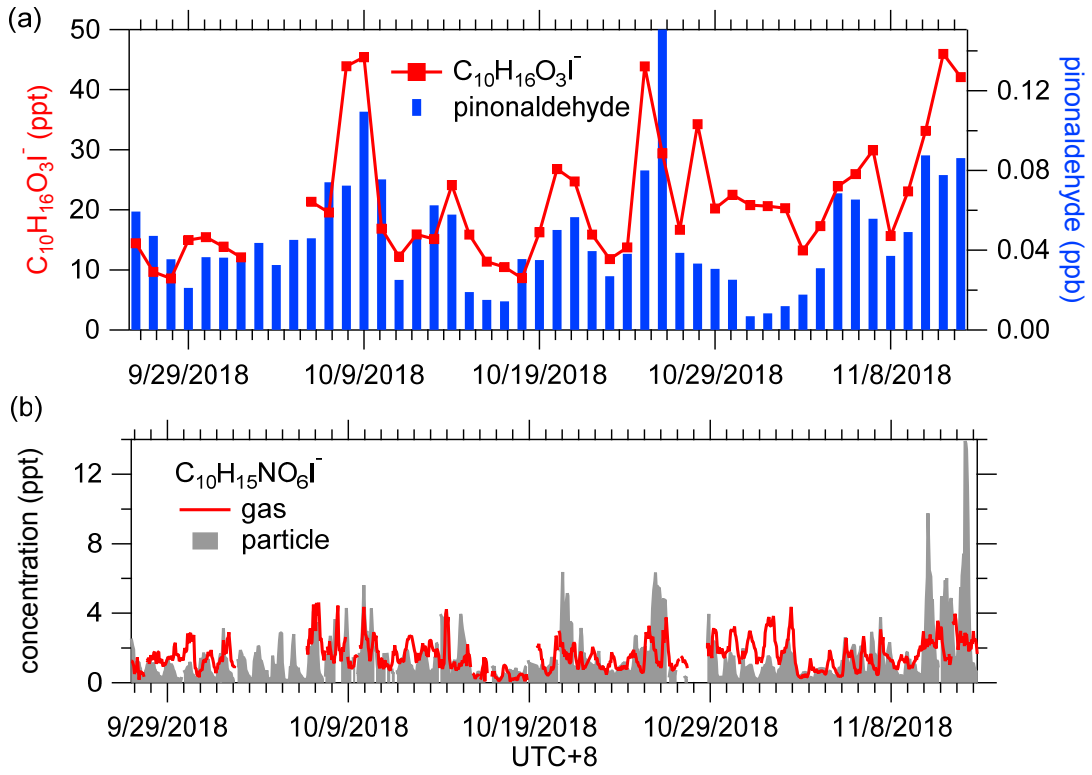

Figure S13. (a) Time series of daily maximum concentrations of gaseous $C_{10}H_{16}O_3I^-$ and pinonaldehyde ($C_{10}H_{16}O_2H^+$, m/z 169.12). (b) Time series of $C_{10}H_{15}NO_6I^-$ in both phases.

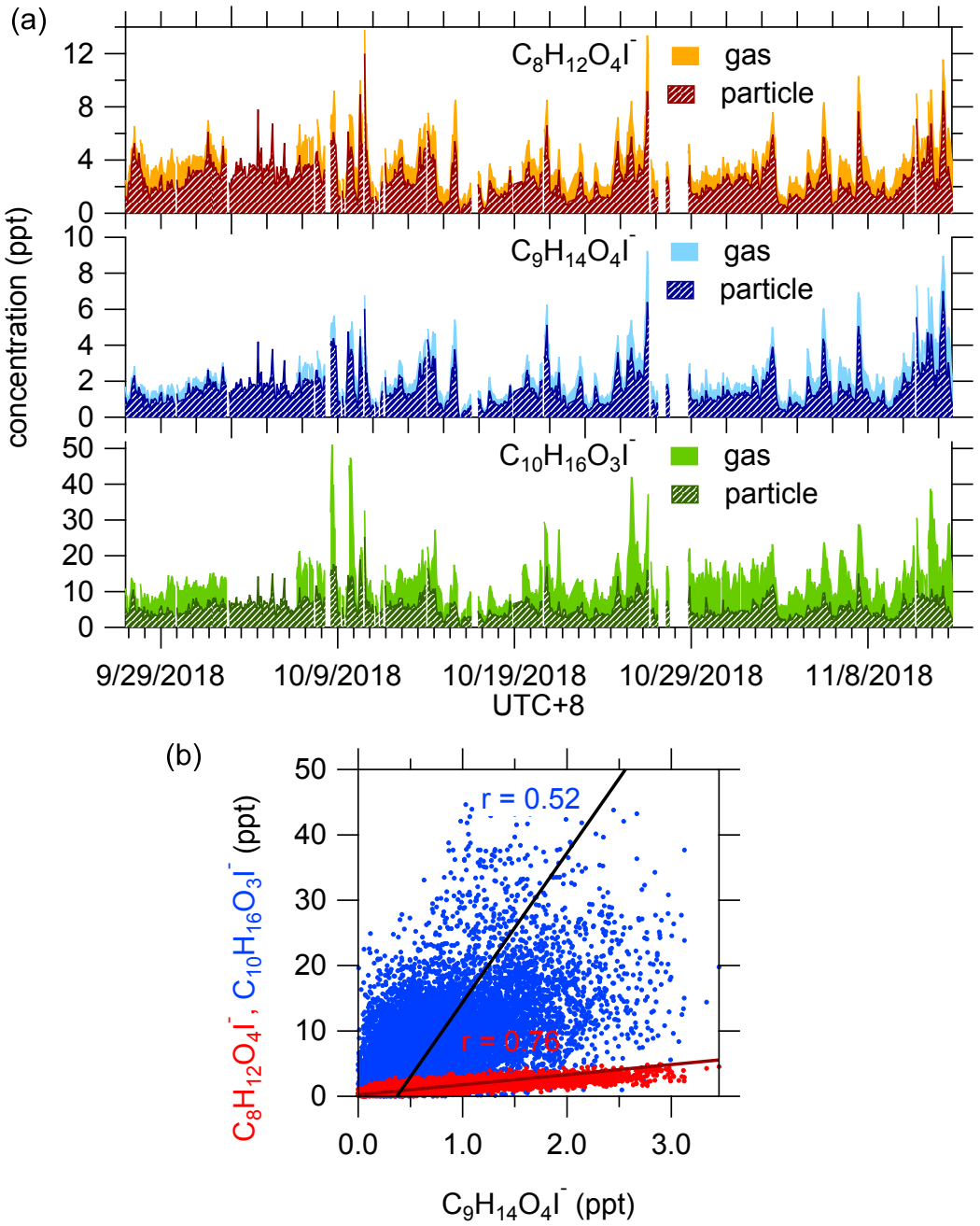

198

199 **Figure S14.** (a) Time series of three oxidation products of monoterpenes. (b)

200 Scatterplots between $C_8H_{12}O_4I^-$, $C_{10}H_{16}O_3I^-$ and $C_9H_{14}O_4I^-$ in the gas phase.

201

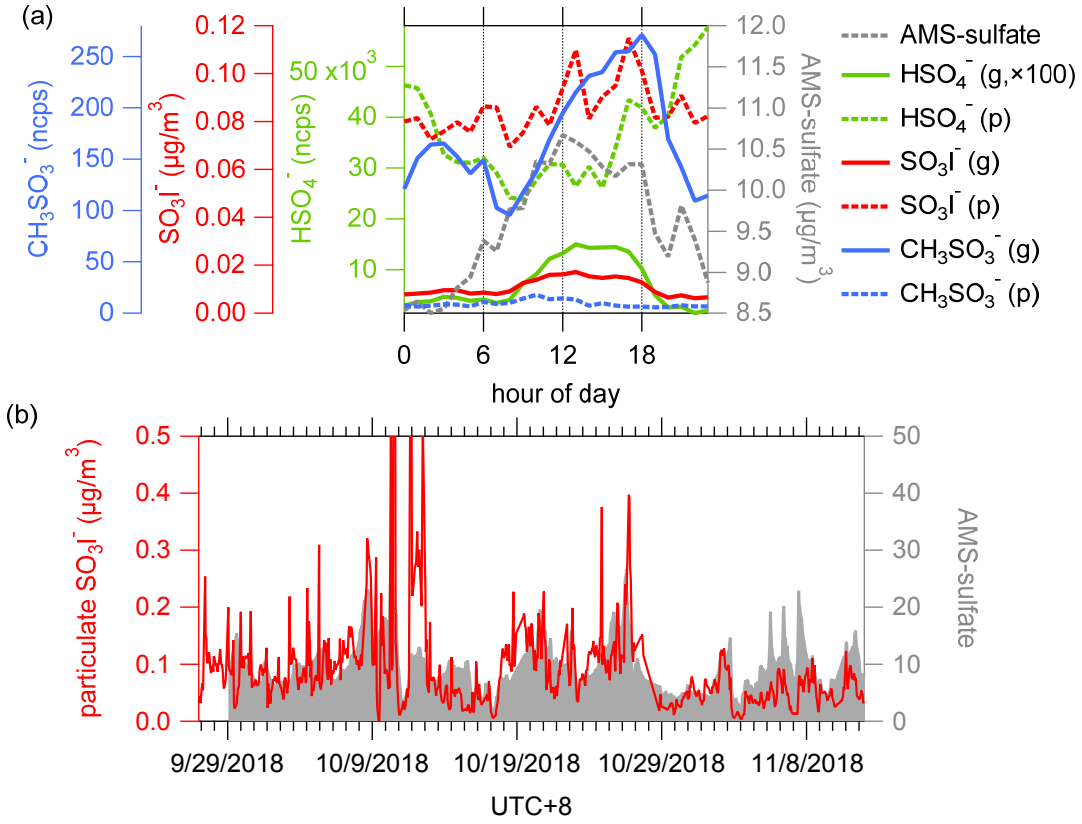

Figure S15. (a) Diurnal trends of S-containing ions measured by FIGAERO-I-CIMS including $CH_3SO_3^-$, SO_3I^- and HSO_4^-, as well as particulate sulfate measured by AMS. (b) Time series of particle-phase SO_3I^- and sulfate.

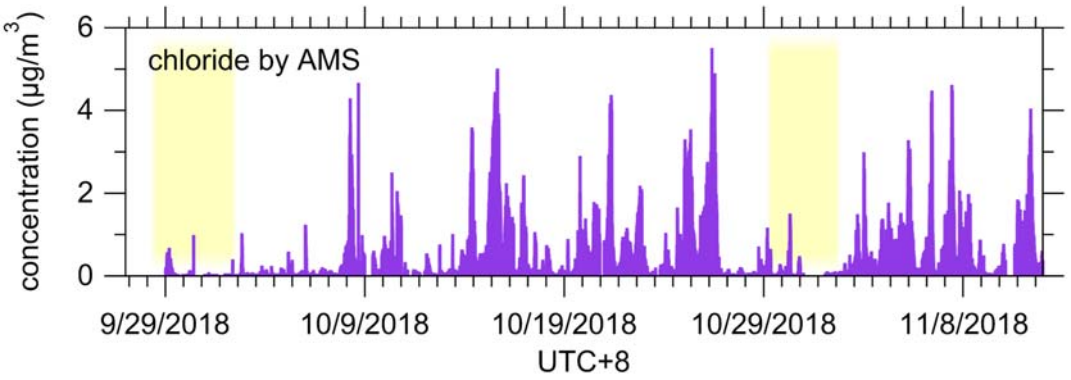

Figure S16. Time series of chlorine measured by AMS.

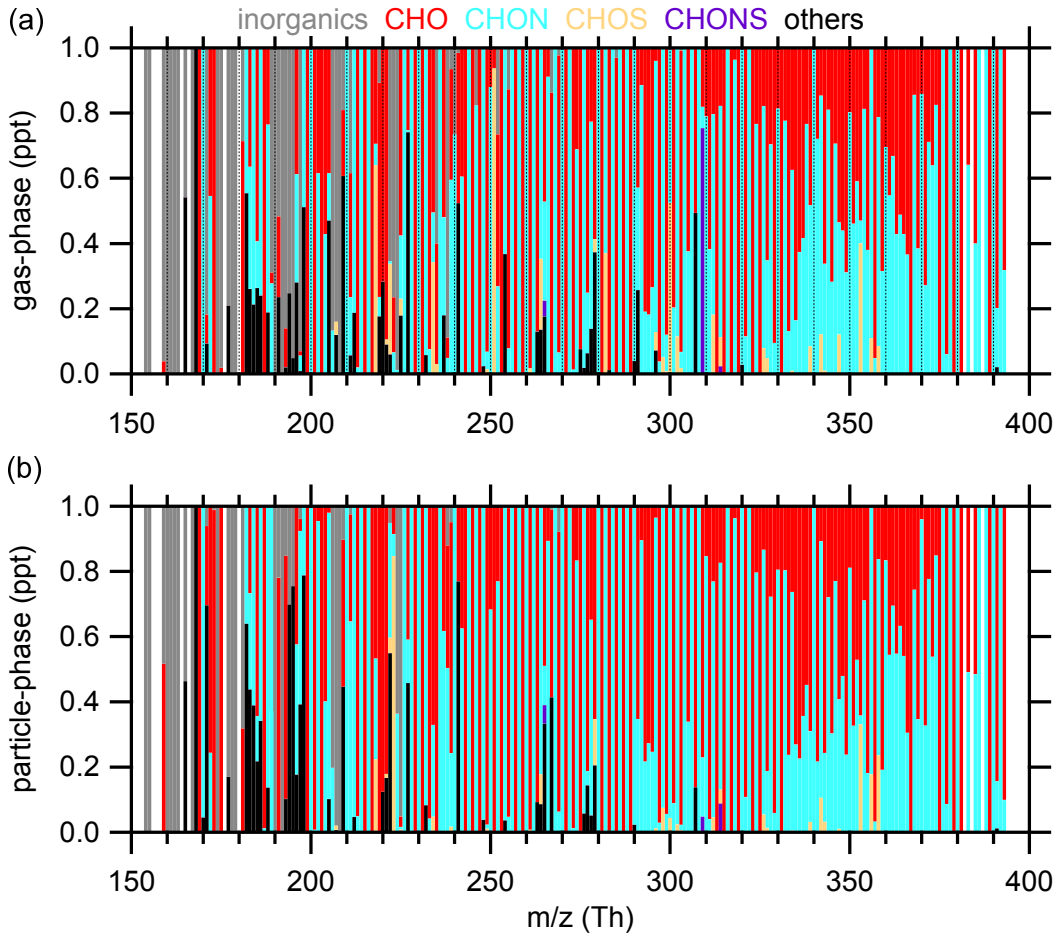

Figure S17. Fractions of species classes for iodide charged ions as a function of m/z in the gas phase (a) and particle phase (b). The concentration of every ion is summed to unit mass resolution to give an overall picture.

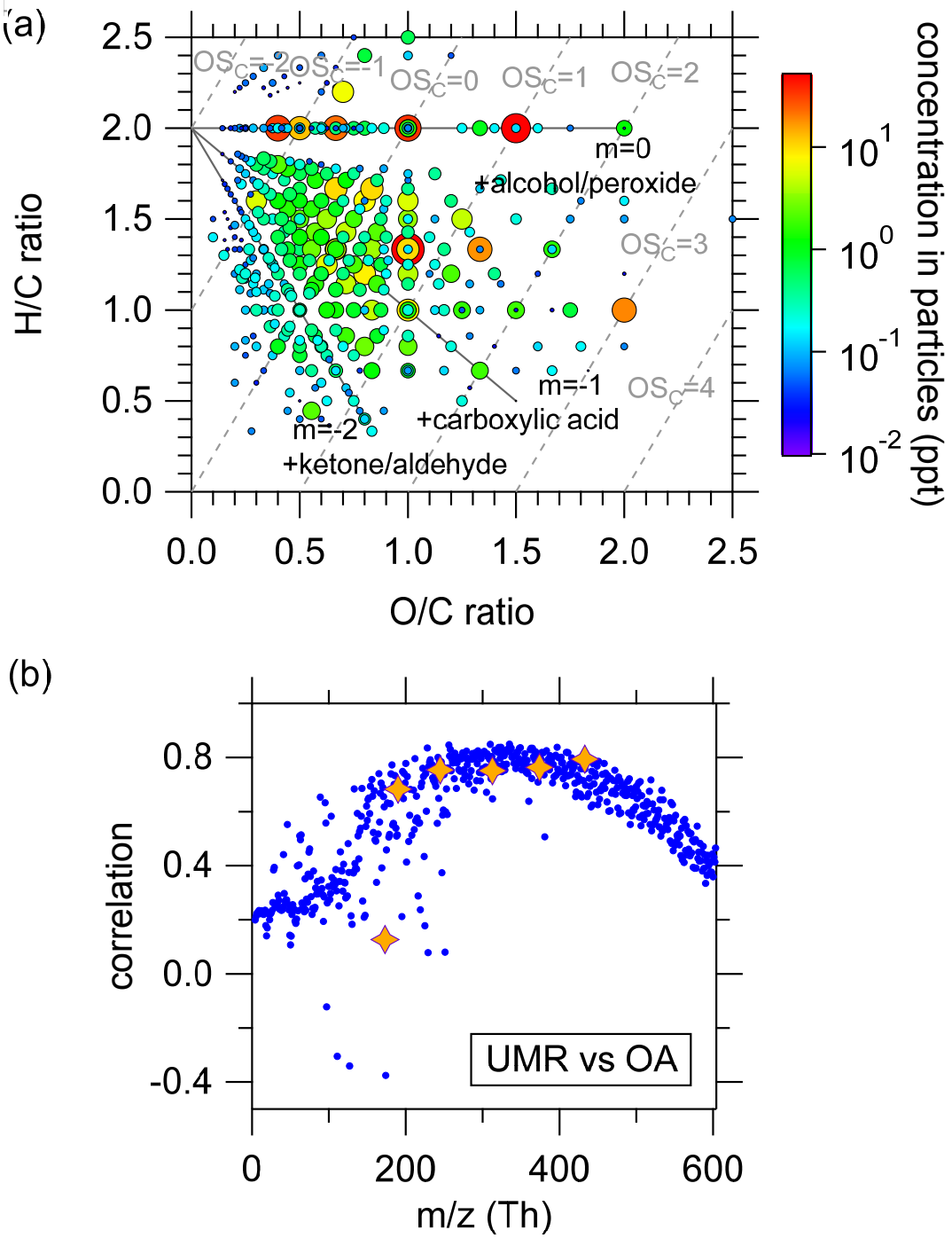

Figure S18. (a) Van Krevelen diagrams for particle-phase $C_xH_yO_z$ compounds detected by FIGAERO-I-CIMS. The size of circles represents the campaign-averaged concentration of this compound in particles. (b) Correlation coefficients between OA and particle-phase UMR signals measured by FIGAERO-I-CIMS, plotted as a function of m/z. Star markers from left to right denote $CH_2O_2I^-$, HNO_3I^-, $C_4H_6O_4I^-$, $C_9H_{14}O_4I^-$, $C_9H_{13}NO_7I^-$ and $C_{10}H_{14}N_2O_9I^-$.